ADVANCED MATERIALS TECHNOLOGIES
www.advmattechnol.de

Fully Inkjet-Printed, 2D Materials-Based Field-Effect Transistor for Water Sensing

*Xiaoyu Sui, Sonal V. Rangnekar, Jaesung Lee, Stephanie E. Liu, Julia R. Downing, Lindsay E. Chaney, Xiaodong Yan, Hyun-June Jang, Haihui Pu, Xiaoao Shi, Shiyu Zhou, Mark C. Hersam, and Junhong Chen**

Despite significant progress in solution-processing of 2D materials, it remains challenging to reliably print high-performance semiconducting channels that can be efficiently modulated in a field-effect transistor (FET). Herein, electrochemically exfoliated MoS_2 nanosheets are inkjet-printed into ultrathin semiconducting channels, resulting in high on/off current ratios up to 10^3. The reported printing strategy is reliable and general for thin film channel fabrication even in the presence of the ubiquitous coffee-ring effect. Statistical modeling analysis on the printed pattern profiles suggests that a spaced parallel printing approach can overcome the coffee-ring effect during inkjet printing, resulting in uniform 2D flake percolation networks. The uniformity of the printed features allows the MoS_2 channel to be hundreds of micrometers long, which easily accommodates the typical inkjet printing resolution of tens of micrometers, thereby enabling fully printed FETs. As a proof of concept, FET water sensors are demonstrated using printed MoS_2 as the FET channel, and printed graphene as the electrodes and the sensing area. After functionalization of the sensing area, the printed water sensor shows a selective response to Pb^{2+} in water down to 2 ppb. This work paves the way for additive nanomanufacturing of FET-based sensors and related devices using 2D nanomaterials.

1. Introduction

2D materials have attracted significant research interest for sensing applications. Their excellent electronic properties, large specific surface area, and chemical robustness enable sensors with unprecedented sensitivity, stability, and fast response. In particular, 2D material-based field-effect transistor (FET) sensors have the advantages of high sensitivity, facile electrical readout, and compatibility with the integrated circuit technology. This class of sensors has already exhibited outstanding capabilities in chemical, biological, mechanical, and optical sensing.[1–4] However, the sensor device cost remains high due to conventional material synthesis and device fabrication techniques used to produce these sensing devices. In many reports, the ultrathin, single-2D nanosheet channels were obtained by mechanical exfoliation of bulk crystals,[5–8] which is a

X. Sui, H.-J. Jang, H. Pu, X. Shi, J. Chen
Pritzker School of Molecular Engineering
University of Chicago
Chicago, IL 60637, USA
E-mail: junhongchen@uchicago.edu

X. Sui, H.-J. Jang, H. Pu, J. Chen
Chemical Sciences and Engineering Division
Physical Sciences and Engineering Directorate
Argonne National Laboratory
Lemont, IL 60439, USA

The ORCID identification number(s) for the author(s) of this article can be found under https://doi.org/10.1002/admt.202301288

DOI: 10.1002/admt.202301288

X. Sui, S. V. Rangnekar, S. E. Liu, J. R. Downing, L. E. Chaney, X. Yan, M. C. Hersam
Department of Materials Science and Engineering
Northwestern University
Evanston, IL 60208, USA

J. Lee, S. Zhou
Department of Industrial and Systems Engineering
University of Wisconsin–Madison
Madison, WI 53706, USA

J. Lee
Wm Michael Barnes '64 Department of Industrial and Systems Engineering
Texas A&M University
College Station, TX 77843, USA

M. C. Hersam
Department of Chemistry
Northwestern University
Evanston, IL 60208, USA

M. C. Hersam
Department of Electrical and Computer Engineering
Northwestern University
Evanston, IL 60208, USA

low-yield and time-intensive process, or chemical vapor deposition (CVD) of 2D thin films,[9–12] which is both time- and energy-intensive. In addition, expensive cleanroom-based photolithography is often utilized to pattern metal electrodes in contact with the 2D channel. In contrast, solution-processing of 2D nanosheets for printable dispersions enables an alternative manufacturing pathway for low-cost, high-throughput, and reproducible sensor device fabrication.[13,14]

2D materials offer a broad spectrum of electronic characteristics suitable for different FET sensor components, while the dangling-bond-free surface of 2D nanosheets through liquid-phase exfoliation promises high-performance van der Waals (vdW) thin films with well-defined interfaces. For example, graphene inks have been well-established for printing conductive electrodes for a variety of sensor applications.[15–18] In addition, electrochemically exfoliated MoS_2 has recently emerged as a key material for constructing semiconducting MoS_2 FET channels with a high carrier mobility (≈10 cm^2 V^{-1} s^{-1}) and high on/off current ratios up to 10^6 by spin-coating.[19] This exfoliation approach produces large-area, few-layer semiconducting 2H-MoS_2 at a high production volume. However, printed 2D semiconducting FET channels often show lower charge carrier mobility and on/off ratio compared with spin-coated ones,[20,21] or can work well only under electrolytic gating conditions.[22,23] These issues result from the limited gate modulation depth and difficulties in reliably achieving ultrathin percolating networks with 2D flakes over large areas using standard printing techniques.

Among available printing options, the prominent advantages of Drop-on-Demand (DoD) inkjet printing, including digital, maskless patterning, non-contact fabrication, controllable droplet deposition, and minimized material usage, make it one of the most promising and widely used additive manufacturing methods for thin-film transistors (TFTs).[1,24] However, inkjet printing is susceptible to the undesired coffee-ring effect (CRE), which leads to nonuniform material deposition that could compromise electrical performance and device uniformity.[25] For example, Kim et al.[20] reported that the on/off ratio of inkjet-printed MoS_2 TFTs dropped to ≈10^2 compared to ≈10^6 for their spin-coated counterparts. To address film nonuniformities across large areas, researchers have used conventional photolithography to define device geometries with short channel lengths close to the single-flake size (i.e., no more than several micrometers[21,26]), which is beyond the typical inkjet printing resolution of tens of microns. The use of cleanroom processing undermines most of the primary scalability and cost advantages of additive manufacturing. Recently, Okin et al.[27] reported an inkjet-printed 2D material-based FET on a SiO_2/Si substrate with graphene electrodes and MoS_2 semiconducting channel, which is 120 µm long and 18 nm thick, and showed an on/off current ratio of 10^3 under vacuum. The improved semiconducting performance of the >100 µm long MoS_2 channel was attributed to the rapid evaporation of isopropyl alcohol (IPA) solvent during ink droplet drying on the substrate, which greatly suppressed the CRE to result in a uniform thin film deposition. This work highlights the importance of overcoming the CRE in inkjet printing 2D FET devices.

Here, inkjet printing is advanced to fabricate robust, ultrathin MoS_2 semiconducting channels that are hundreds of micrometers long using electrochemically exfoliated MoS_2 nanosheets. The printed MoS_2 channels exhibit an on/off current ratio up to 10^3 under ambient conditions instead of vacuum. Benefiting from the optimized inkjet printing strategy, i.e., multilayered deposition of single-line pattern, the printed ultrathin MoS_2 nanosheet percolation networks are <10 nm thick, which are confirmed by atomic force microscopy (AFM) measurements and further supported by statistical modeling analysis on printed pattern profiles. The long channels are compatible with standard inkjet printing resolution, thereby enabling fully printed FET devices. Exploiting the large-area uniformity, fully functioning water sensors for heavy metal ion detection are demonstrated using printed MoS_2 for the semiconducting channel and printed graphene for the electrodes.

2. Results and Discussion

First, semiconducting MoS_2 ink was developed with specific consideration for the following hallmarks of high-quality inkjet printing: 1) The ink suspension should be stable without solute material aggregation during the printing process. 2) The size of suspended solid materials should be tailored within a certain size range (e.g., <1/10 of the nozzle diameter based on this study) to avoid nozzle clogging. 3) The rheological properties of the ink should be tuned to ensure stable droplet jetting under each electrical drive pulse. The ink rheology is generally evaluated by the inverse Ohnesorge number $Z = \sqrt{\gamma \rho a}\,/\eta$, which depends on the ink viscosity (η), surface tension (γ), and density (ρ), and the printer cartridge nozzle diameter (a). A Z value is expected to be in the range of 1–14 for inkjet-printable inks.[28] 4) Good substrate wetting of the inks is necessary, which requires the ink surface tension to be 7–10 mN m^{-1} lower than the substrate surface energy.[29] 5) Suitable fluidic properties are required to minimize the CRE for uniform material deposition and desirable semiconducting performance. To satisfy the considerations of 1) and 2), PVP-stabilized electrochemically exfoliated MoS_2 was processed and filtered to ensure its stability during printing and its size compatibility with the printer nozzle diameter (details in Experimental Section). To meet criteria 3), 4), and 5), the MoS_2 nanosheets were formulated into printable inks using an IPA/2-butanol (10 vol.%) solvent system, which has a Z value of 10, and sufficiently lower surface tension of ≈28 mN m^{-1} compared to that of the Si/SiO_2 substrate ≈36 mN m^{-1}.[29] Finally, the Marangoni-enhanced spreading observed in this formulation unpins the contact line and deforms the droplet shape to alleviate the CRE.[29,30] The above features make IPA/2-butanol binary solvents a common formulation for inkjet printing of 2D nanosheets.[29,31–33] However, there is debate that a single IPA solvent without the additional 2-butanol works better in suppressing the CRE for MoS_2 nanosheet deposition.[20,27] This lack of consensus reflects the challenge in completely eliminating the CRE during inkjet printing. Therefore, instead of attempting to fully remove the CRE, we sought to optimize the thin 2D semiconducting channels in the presence of the CRE based on the chosen ink formula. This approach has the potential to be more reproducible and general for the realization of thin 2D networks as semiconducting channels.

The ink concentration used for inkjet printing was tuned to 1 mg mL^{-1} of MoS_2 in IPA/2-butanol, and the nanosheet quality was first examined. The MoS_2 nanosheets have a lateral size

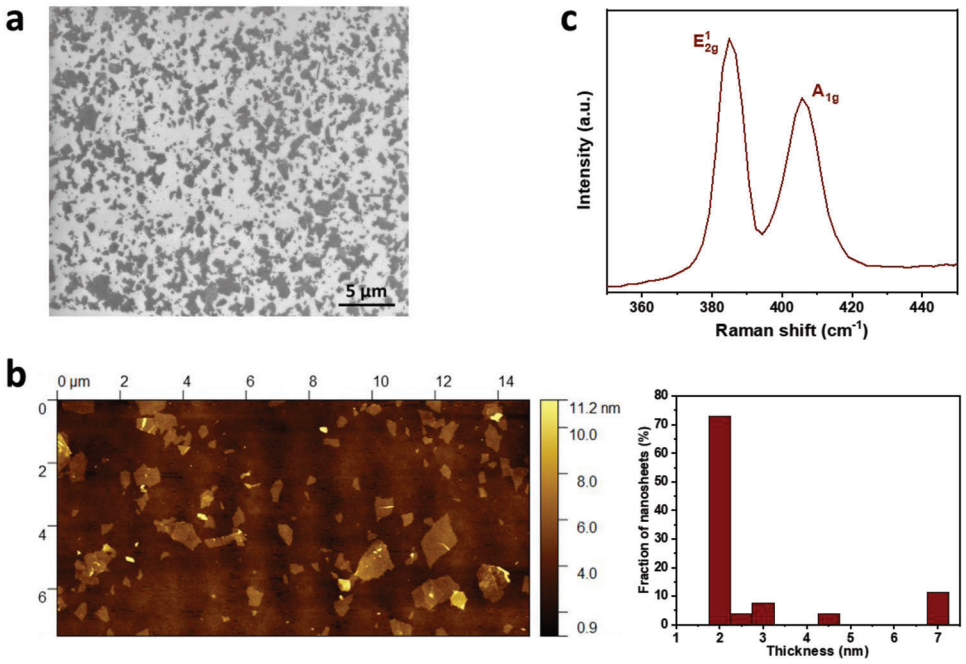

Figure 1. a) Scanning electron microscopy (SEM) image, b) Atomic force microscopy (AFM) image and thickness distribution, and c) Raman spectrum of tetraheptylammonium bromide (THAB)-exfoliated MoS_2 nanosheets in the ink.

within 2 µm and exhibit a narrow thickness distribution peaking at ≈2 nm (two to three-layer MoS_2), although some thicker flakes with a smaller lateral size can be detected (**Figure 1**a,b; Figure S1, Supporting Information). The narrow thickness distribution minimizes the variation in the energy bandgap of the MoS_2 nanosheets, benefiting the FET device performance.[34] Raman peaks of E^1_{2g} and A_{1g} at 384.9 and 405.7 cm^{-1} with a 20.8 cm^{-1} difference in between indicate the two-layer dominating feature of exfoliated MoS_2 nanosheets (Figure 1c),[35] in agreement with the AFM results.

A Fujifilm Dimatix DMP 2850 inkjet printer equipped with a 10-pL cartridge was used to print the MoS_2 ink on a precleaned substrate of 300-nm thick SiO_2 on doped Si. The diameter of individual printed dots is ≈55 µm, and a drop spacing of 40 µm was optimized to print MoS_2 lines, showing uniform edges (**Figure 2**a,d). More materials were deposited on the line pattern edges, presenting the CRE. Channel patterns containing five parallel lines were initially printed for electrical characterization since multiple lines increase the probability of fabricating a percolating electronic pathway compared to single-line printing. To improve electrical conductance, thermal annealing under Ar gas flow was employed to remove the residual solvent and PVP from the printed MoS_2 films as well as improve the contacts among the flakes in the percolating network. Annealing temperatures in the range of 250 to 350 °C were tested, and devices annealed at 350 °C were shown to have the best on/off ratios (back-gate V_g from −38 to 38 V) based on six printing-pass patterns – i.e., 6 layers of ink deposition (Figure 2b; Figure S2, Supporting Information). This higher annealing temperature helps to reduce unintentional impurity doping (e.g., from residual PVP), which shifts the threshold voltage in the positive direction.[19] The optimal annealing temperature also coincides with the thermal decomposition of PVP starting at ≈350 °C,[21] and thermogravimetric analysis confirmed that dwelling at 350 °C does partially remove PVP (Figure S3, Supporting Information). For thinner parallel line patterns with fewer printing passes, a percolating network was formed at two printing passes but was too resistive (on the order of 10^{10} Ohm) to produce a stable transfer curve. With four printing passes, a weak on/off ratio <2 was achieved. We noticed a rapid film thickness increase during multi-line printing due to the overlapping deposition along adjacent parallel lines (e.g., the darker regions in Figure 2a). Thick films introduce increased electrostatic screening that sacrifices the gate modulation of the printed MoS_2 channel.

In order to improve the on/off current ratio, single-line patterns were printed to achieve thinner percolating networks. The AFM image on the edge of the single-pass printing pattern in the inset of Figure 2c indicates that the CRE persists as a major challenge in inkjet printing and could not be removed completely through the chosen solvent formulation. Nevertheless, the CRE can be advantageously utilized to produce two parallel conductive channels at the edges of the printed line. The edge thickness increases with the printing passes, starting from ≈3.8 nm for one printing pass to ≈12 nm for eight printing passes as shown in Figure 2c. Percolating networks can be prepared from four printing passes with an edge thickness ≈7 nm, which increases to ≈10 nm for six printing passes (Figure 2d,e). As expected, the on/off current ratio decreases with increasing printing passes, which increases the film thickness, from an initial on/off ratio of ≈10 for four printing passes to ≈2 for eight printing passes (Figure 2f), because the thicker film favors a higher off current due to the limited gate modulation depth. However, thinner channels with higher on/off ratios have a larger performance variation and a limited device yield since they are so close to the

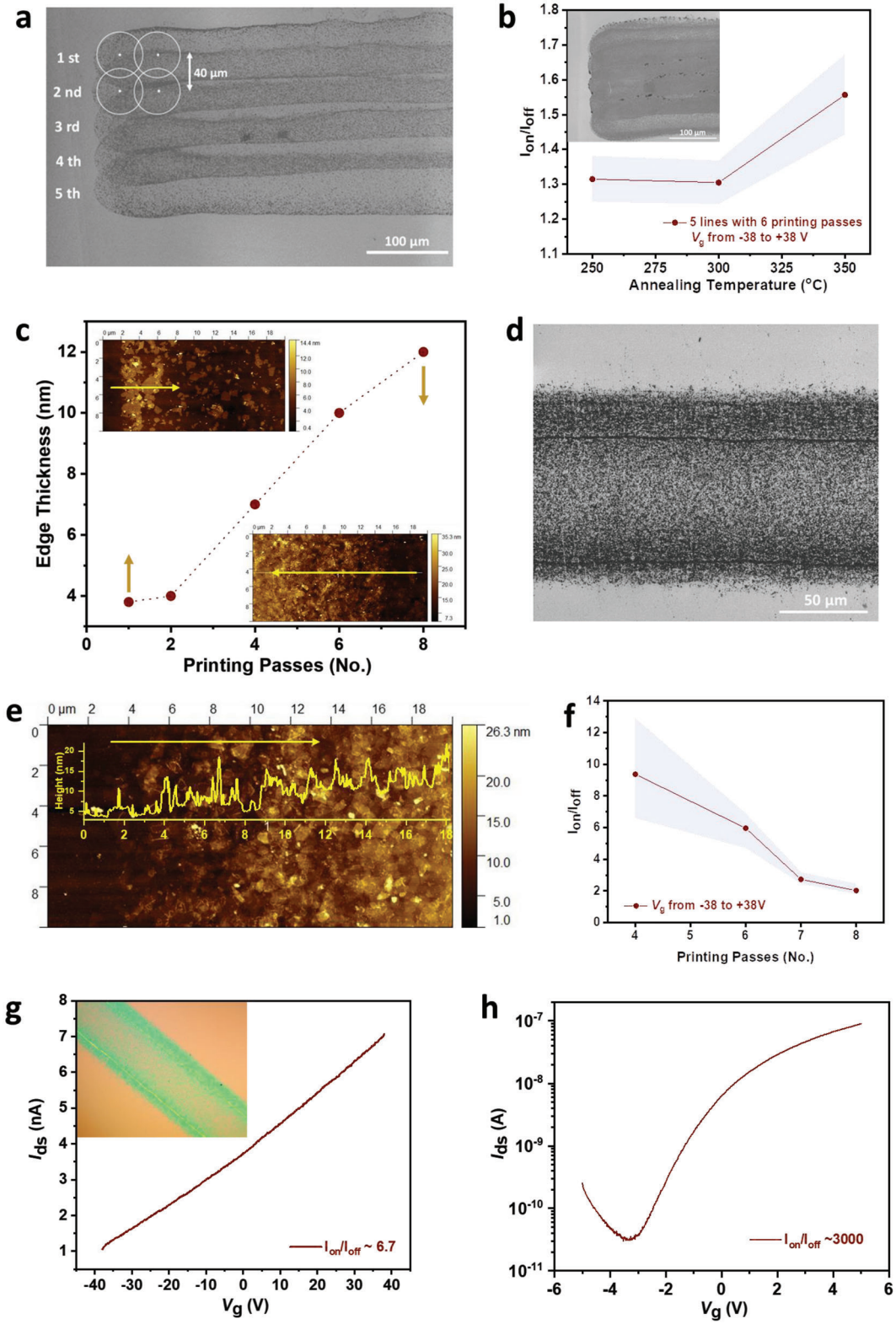

Figure 2. a) SEM image of inkjet-printed single-layer MoS_2 patterns containing five parallel lines with an optimized drop spacing of 40 μm. b) On/off current ratio as a function of annealing temperature. c) Edge thickness vs. printing passes with AFM images on the edges of one printing pass and eight printing passes (horizontal arrows pointing to the line pattern center) in the inset. d) SEM image and e) AFM profile on the edge of printed MoS_2 single line pattern with six printing passes (the horizontal arrow pointing to the line pattern center). f) On/off current ratio of MoS_2 single line pattern vs. printing passes. A typical transfer curve of MoS_2 single line pattern with six printing passes on g) a 300 nm-SiO_2/Si substrate and h) an ALD deposited 24 nm-AlO_x/Si substrate.

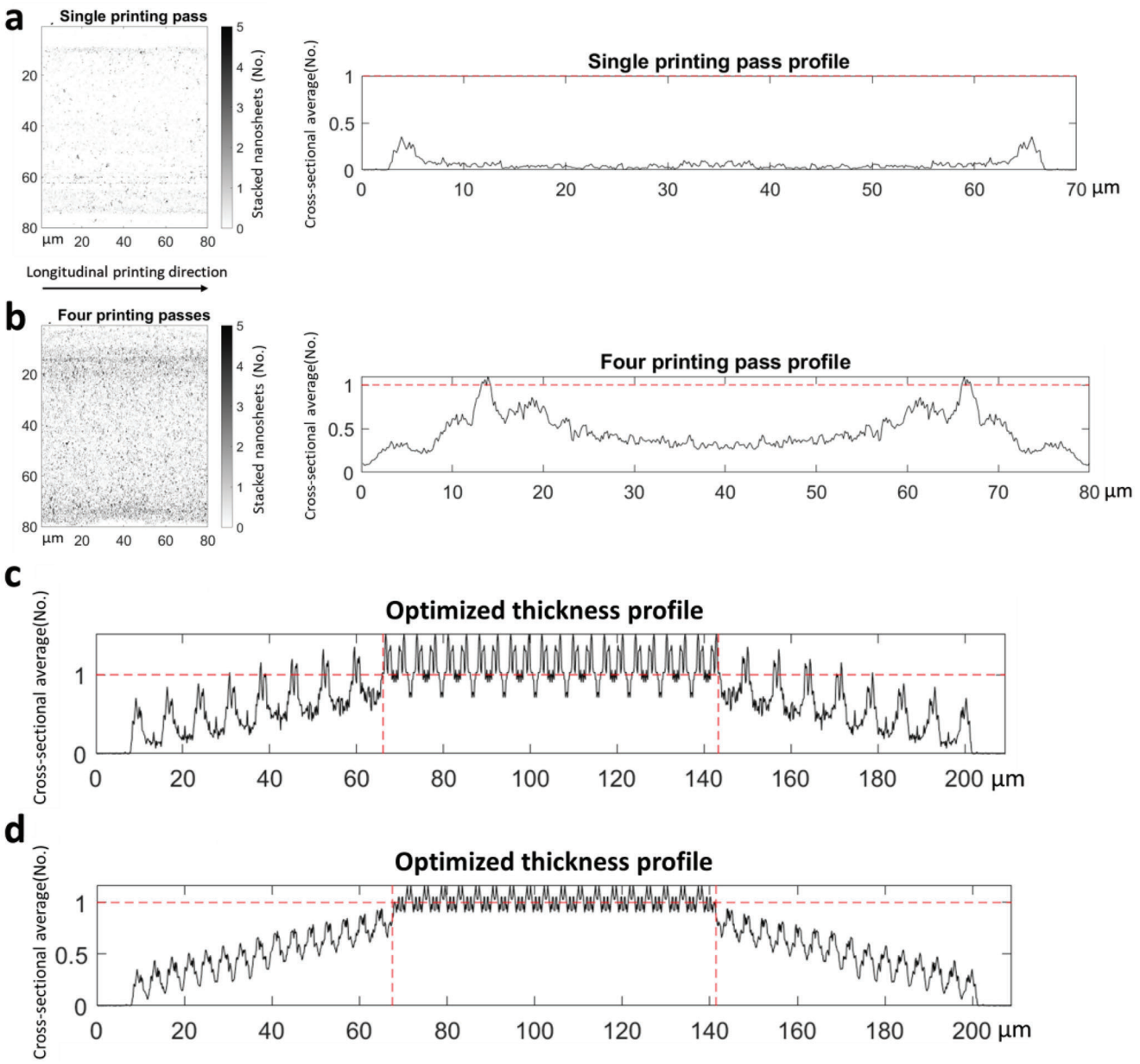

Figure 3. Preprocessed AFM images of single line patterns with thickness represented by the number of stacked MoS_2 nanosheets (left) and average cross-sectional thickness profiles (right) for a) one printing pass and b) four printing passes. To simplify the mathematical analysis, we mirrored the left half profile data (collected from the top half of the AFM images) to the right. c) The optimized average thickness profile of the MoS_2 channel with two printing-pass 18 parallel lines, spaced by 7.2 μm. The center region of interest is indicated with two vertical dashed lines. d) The optimized average thickness profile of the MoS_2 channel with single-printing-pass 33 parallel lines, spaced by 3.9 μm.

percolation threshold that an electrically percolating network is not always achieved. For example, MoS_2 channels with four printing passes exhibit a higher on/off current ratio but a larger variation and significantly lower yield ≈50% (the others are open circuits) compared with thicker channels from more printing passes (having ≈100% device yield).

To balance the trade-off between on/off ratio and device uniformity as well as to guarantee a high device yield, semiconducting channels with ≈10 nm thickness from six printing passes, which produce on/off ratios ≈6, were chosen for further FET water sensor fabrication. A typical transfer curve of a 6-pass printed channel is shown in Figure 2g, exhibiting an n-type semiconducting output. To evaluate the ultimate on/off current ratio of the printed MoS_2 channel, an atomic layer deposited 24 nm-AlO_x/Si substrate was used for more efficient gate modulation. In this case, an on/off ratio on the order of 10^3 was observed (Figure 2h), which is three orders of magnitude lower than the intrinsic on/off ratio of a single exfoliated MoS_2 flake on the order of 10^6 (Figure S4, Supporting Information), but among the top-ranking performances reported for inkjet-printed

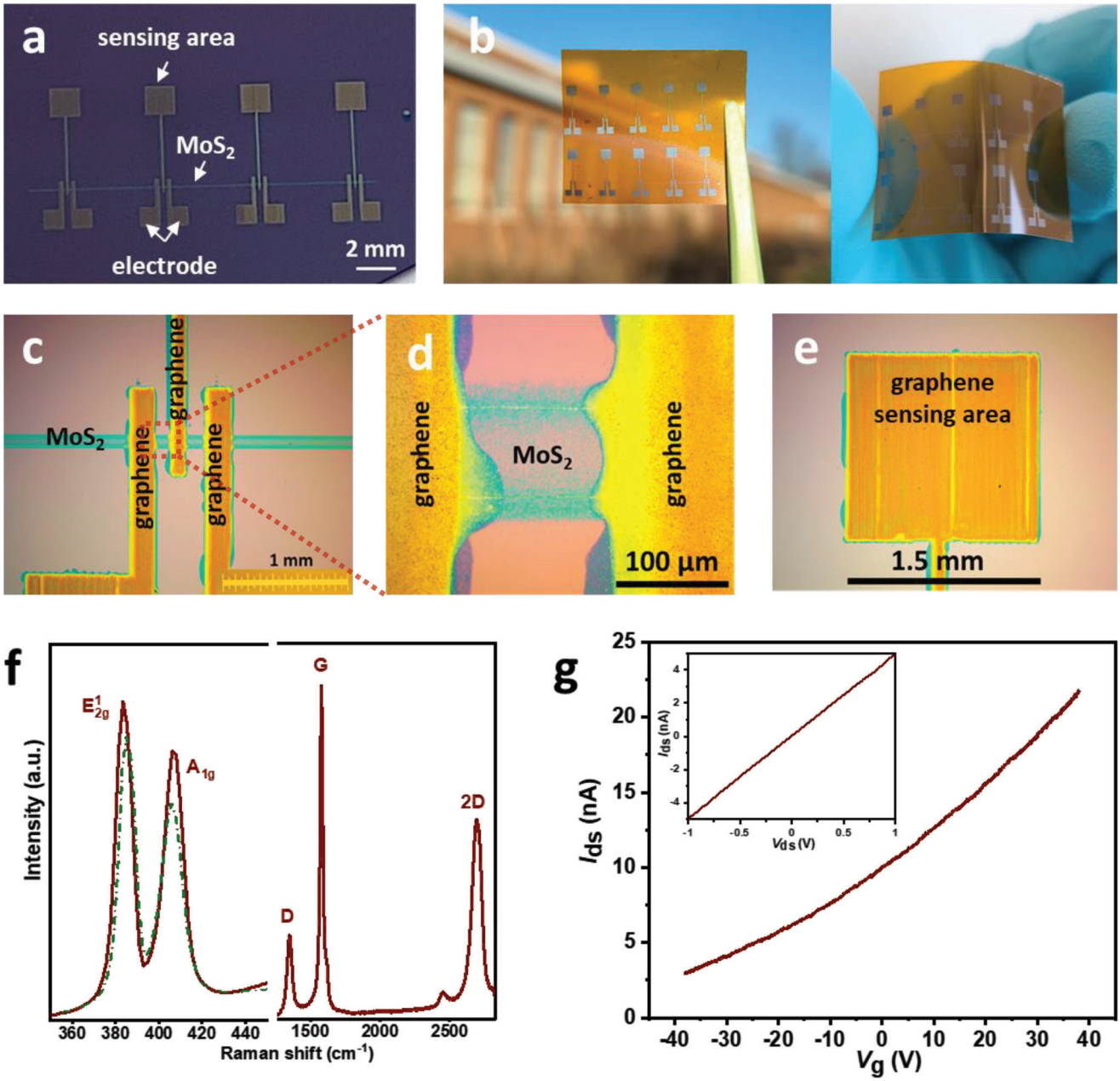

Figure 4. a) Fully inkjet-printed sensor devices on Si wafer and b) polymer substrate. c-e) Optical images, f) Raman spectra of MoS_2 (left with dotted one from single flakes) and graphene (right), and g) transfer curve, with output *I–V* curve in the inset, of the sensor device on SiO_2/Si.

2D semiconductor channels on substrates that employ an oxide dielectric,[20,27] as illustrated in Table S1 (Supporting Information). The field-effect mobility achieved in our printed MoS_2 is estimated to be ≈0.27 $cm^2\ V^{-1}\ S^{-1}$, surpassing the values reported in previous solution-processed MoS_2 transistors,[22,36] by using the equation: $\mu = \frac{L}{WC_{ox}V_{ds}}\frac{dI_{ds}}{dV_g}$ where $\frac{dI_{ds}}{dV_g}$ is the slope of the transfer curve; $C_{ox} = 3.03 \times 10^{-7}$ F cm^{-2} is the gate capacitance for a 24-nm AlO_x/Si substrate;[37] $V_{ds} = 1$ V is the drain-source voltage; $L = 400$ µm and $W = 100$ µm are used as the semiconducting channel length and width, respectively (device dimensional details are shown in Figure 4). It should be noted that the actual channel width is much smaller than the width of the printed line pattern (≈100 µm), since the MoS_2 percolating networks only form on the two edges of the line pattern. Thus, the actual carrier mobility is considerably higher. It has been reported that bis(trifluoromethane)sulfonimide (TFSI) treatment could remove possible impurities and passivate sulfur vacancies in the electrochemically exfoliated MoS_2 flakes, and thus further increase the charge carrier mobility.[19,20,27,38] Moreover, measurements in vacuum can further enhance mobility. However, for the purpose of FET-based sensors, mobility is not a primary consideration and thus further optimization of this metric was not performed here.

A data-driven mathematical analysis was conducted to understand the formation of 2D flake percolating networks during printing and to further investigate the optimal printing strategy to obtain stable, thin percolating channels in the presence of CRE. First, the average cross-sectional thickness profiles over the longitudinal direction of the printed single line patterns are obtained from the AFM images. The thickness profiles are then converted into the number of stacked MoS_2 nanosheets with the assumption that a single MoS_2 nanosheet thickness is 2 nm (Figure 1b). This conversion demonstrates that nanosheet percolation forms upon four printing passes: the maximum stacked sheet number for the one printing pass profile (named baseline profile) is 0.354, much <1, which means the channel is covered by less than one layer of MoS_2 nanosheets on average and thus is unlikely to achieve a percolation network by a single printing pass (**Figure 3**a); in contrast, the four printing pass profile (Figure 3b) has a maximum average stacked sheet number of 1.096, >1, which is on the border of percolating network formation. Since the sheet number peaks for four printing passes are very close to one and only within two narrow edges, implying the printed network is approaching the percolation threshold,[39] the device yield is limited to ≈50% as observed. It is noteworthy that the preprocessed average cross-sectional thicknesses of printed patterns are smaller than those from the line profile measurement in Figure 2c, indicating thickness variations exist along the longitudinal printing direction that may cause failure in achieving network percolation. Thus, the average values here are more efficient to describe the percolating behavior of printed 2D nanosheets.

The observed semiconducting performances of printed MoS_2 channels expose a dilemma that a thinner percolation network results in a higher on-off current ratio, but the device yield will be lower (Figure 2c,f). This tradeoff can in part be attributed to the ubiquitous CRE during printing that leads to the uneven material deposition of only two narrow, thicker networks on the two edges (less chance to achieve percolation than uniform thin films). Further mathematical modeling efforts reveal a spaced parallel printing strategy (i.e., print parallel lines abreast with overlaps) to accommodate this issue and achieve a wider, thin channel that has a stable percolation network (details in Figures S5 and S6, Supporting Information). The printer has a minimum controllable drop spacing of 5 μm (i.e., the minimum center-to-center distance from one drop to the next for ink deposition). Using this minimum controlling drop spacing as a constraint, the modeling results reveal that printing parallel lines with an optimal distance of ≈7 μm and two printing passes for each line patterns should result in a uniform, thin, width-adjustable, and stable percolating network in the center of the printed channel as shown in Figure 3c. These printing conditions can improve both the semiconducting performance and the yield of prepared devices, because it is thinner than a single-line pattern with six printing passes chosen for the FET device fabrication and close to the thickness from four printing passes, while concurrently resulting in a wider channel that increases the possibility of achieving percolation. This printing strategy is an effective and general way to contend with the CRE for a uniform deposition during nanomaterial printing fabrication. Improvements in the minimum controllable drop spacing provide further options for achieving reliable percolating networks with a flatter and thinner center region through only one printing pass as shown in Figure 3d with ≈4 μm drop spacing as an example.

After printing the MoS_2 semiconducting channel, source/drain electrodes and an extended sensing area were further printed using well-established graphene inks.[40–44] The chemical inertness of graphene electrodes can avoid unwanted chemical degradation at the MoS_2/contact interface.[45] After moderate thermal annealing at 350 °C, a fully inkjet-printed FET-based water sensor device is fabricated (**Figure 4**a), which can also be mechanically flexible when printed onto polymer substrates, e.g., polyimide (70 μm thick) as shown in Figure 4b. Bending tests along the MoS_2 channel length were performed to investigate the mechanical stability of the printed flexible device. A stable device resistance can be well kept after 1 000 bending cycles at a radius of curvature of 13.5 mm and successive 500 bending cycles at a radius of curvature of 7.9 mm (Figure S7a, Supporting Information). There is no visible morphology change of the device after the bending test, suggesting a strong affinity of the printed 2D materials with the polyimide substrate, which could contribute to the mechanical stability of the flexible devices (Figure S7b, Supporting Information). Sensor device arrays can be readily achieved through printing pattern design, demonstrating excellent scalability. The dimensions and printing quality of the device are exhibited in Figure 4c–e. The MoS_2 channels bridging the source/drain electrodes are designed to be 400 μm long (Figure 4c) to accommodate the printing resolution and possible graphene ink diffusion along the pre-printed MoS_2 channels during electrode printing (Figure 4d). A graphene sensing area was connected and extended several millimeters away from the MoS_2 channel to avoid the interference of the analyte onto the circuit during sensing tests. In Figure 4f, the distance of two characteristic Raman peaks of the printed MoS_2 channel becomes wider compared with exfoliated single flakes, indicating their stacking overlap to form a percolation network, while the 2D, G, and D bands from printed graphene electrodes present characteristics of multi-layer graphene.[46] In combination with graphene electrodes, the semiconducting property of the MoS_2 channel is maintained as shown in Figure 4g, and the linear I–V curve shown in the inset confirms ohmic electrical contact between the MoS_2 channel and the graphene electrodes. As a proof of concept for device application, the extended graphene sensing area of the fabricated FET device was functionalized with 1-pyrenebutyric acid through π-π interaction for selective lead ion detection using an aqueous solution-gated setup (**Figure 5**a). As shown in Figure 5b, much more efficient top-gate modulation upon the FET device (i.e., much higher on/off current ratio) is observed compared with the bottom-gate modulation (i.e., bottom gate from the silicon wafer), showing an inverse transfer curve output. The exhibited much higher on/off current ratio 6.319 via top-gate modulation vs. 1.006 via bottom-gate modulation with V_g ranging from −0.5 to 0.5 V confirms the intrinsic good semiconducting property of the printed MoS_2 FET channel, which is essential for a highly sensitive detection through top-gate configuration.[5] The inverse output is likely due to the direct contact of the graphene sensing area with the MoS_2 channel as shown in Figure 5a. When a positive V_g was applied through the analyte, which causes the ions to migrate and accumulate at the gate-analyte and analyte-graphene interfaces, i.e., forming two "electrical double layers" (EDLs).[47]

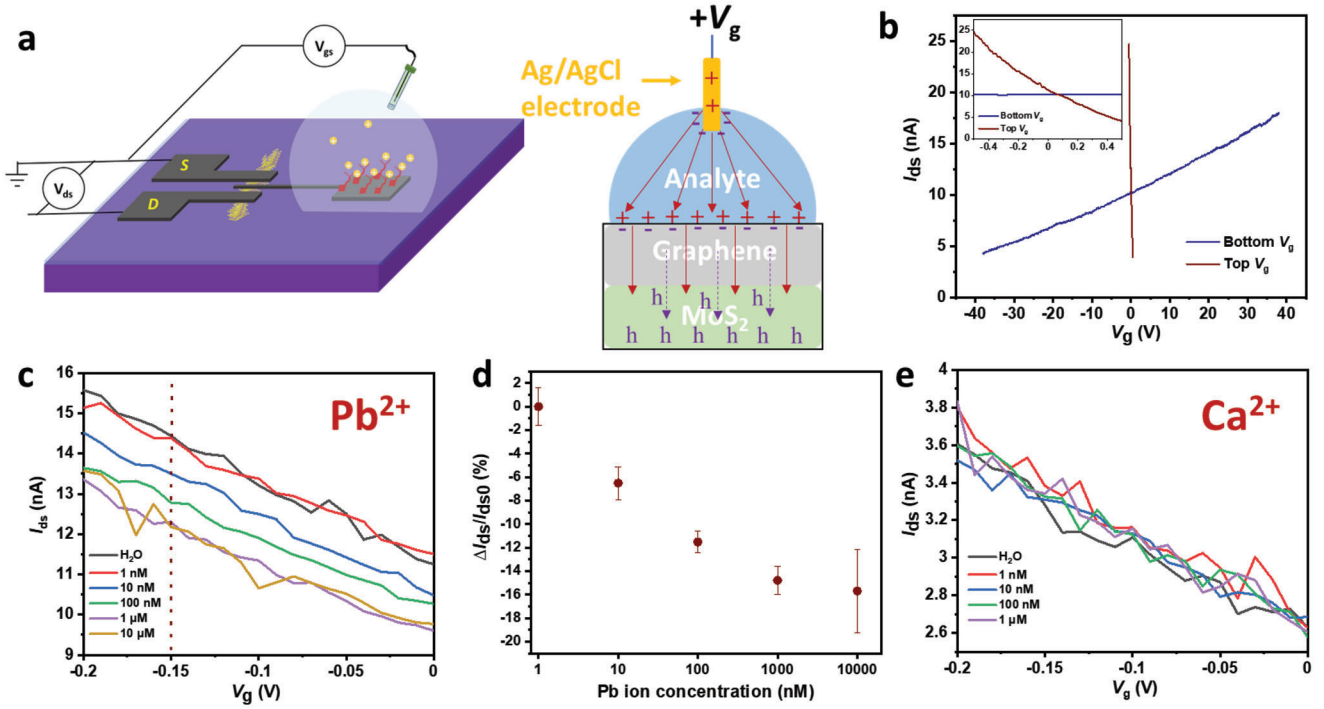

Figure 5. a) Schematic of sensing test and charge transfer upon positive V_g. b) Transfer curves of the same device upon top/bottom V_g with a zoom-in plot in the inset. c) Water sensor responses to Pb^{2+} in water and d) calculated sensitivity according to I_{ds} at $V_g = -0.15$ V (top gate) as indicated with the dotted line in figure (c). The error bars illustrate the response curve fluctuations accordingly. e) Sensing response to Ca^{2+} in water.

The semi-metallic graphene layer will shield the electric fields from the top-gate electrode by repulsing its holes into the underlying MoS_2. The work functions of MoS_2 and graphene are comparable, thus the Fermi level of graphene lies within the conduction and valence bands of MoS_2,[48–50] supporting this charge transfer. The injected holes decrease the MoS_2 channel conductance for a lower current output.

The sensor device was exposed to different Pb ion concentrations, and top V_g scans were applied to the sensor device until a stable transfer curve output was obtained (within a few minutes) as the sensing signal in response to individual Pb^{2+} concentrations. The sensor initially responded at 10 nM (i.e., ≈2 ppb) of Pb^{2+} with a sensing response (i.e., $\Delta I_{ds}/I_{ds0}$) of 6.5%, and became saturated around 1 μM (i.e., ≈200 ppb), as shown in Figure 5c,d. Common cations present in water including Ca^{2+}, Mg^{2+}, and Na^+ have been used to evaluate the selectivity of water sensors; no obvious sensing response was measured for these interfering cations (Figure 5e; Figure S8, Supporting Information). It is believed that the functionalized —COOH of 1-pyrenebutyric acid on the sensing area coordinates with Pb^{2+} at the interface between the analyte and the graphene sensing area,[39,51] inducing an additional positive gate voltage, which decreased the I_{ds} according to the inverse transfer curve (top V_g configuration in Figure 5b).

3. Conclusion

Due to the CRE during inkjet printing, two edges of the line pattern effectively form the percolating networks initially. By taking advantage of this feature, a printing strategy of single-line pattern with multilayered deposition was used to fabricate ultrathin, robust MoS_2 semiconducting channels, and an on/off current ratio up to 10^3 has been realized in printed FETs. This printing strategy utilizing CRE is general and feasible for ultrathin 2D conductive channel construction with a given ink formulation. Further statistical modeling analysis suggested a spaced parallel printing approach as another approach to achieve uniform 2D flake percolation networks even for inks that show the CRE. The printed MoS_2 channel can be hundreds of micrometers long, which is compatible with inkjet printing resolution and facilitates a fully printed FET device. As a proof of concept for device application, a fully functioning FET-based water sensor with an extended sensing area has been fabricated based on the printed MoS_2 semiconducting channel and graphene electrodes. After 1-pyrenebutyric acid functionalization, the water sensor showed a selective response to Pb^{2+} in water with a concentration as low as 2 ppb. This work can likely be generalized to other FET-based devices, thereby increasing the application potential of 2D materials in additive manufacturing.

4. Experimental Section

Chemicals: For the MoS_2 ink, a synthetic single crystal (2D Semiconductors, USA) was first electrochemically intercalated by tetraheptylammonium bromide (THAB) in acetonitrile and stabilized by polyvinylpyrrolidone (PVP; MW: 29 kDa) in isopropyl alcohol (IPA) following a previously published protocol.[19] To remove unexfoliated material, the dispersion was centrifuged in a Beckman Coulter JS-7.5 rotor at 7 500 rpm for 5 min. The supernatant was retained as a viable MoS_2 dispersion. To formulate an inkjet-printable ink, the MoS_2/IPA dispersion was first filtered through

a 1 µm glass fiber syringe filter. The rheology of the ink was adjusted by adding 2-butanol to a final IPA : 2-butanol volume ratio of 9:1; this solvent system has been demonstrated by Hu et al.[29] to be robust for inkjet printing. The final ink concentration was finalized to be ≈1 mg mL^{-1}, which was confirmed by UV–vis spectroscopy. The graphene ink was prepared as previously reported.[18] Metal chloride or nitrate salts used to prepare metal ion solutions with deionized (DI) water were all purchased from Sigma–Aldrich.

Sensor Device Fabrication by Inkjet Printing: The MoS_2-IPA/2-butanol ink was used to print an MoS_2 percolating network as the semiconducting channel, and the graphene ink was used for printing conductive electrodes onto SiO_2 (300 nm)/Si wafers or polyimide substrates (#300NH from DuPont). The substrates were pre-cleaned by acetone, IPA, and DI water with sonication for 10 min, respectively, prior to material deposition. A Fujifilm Dimatix DMP 2850 inkjet printer equipped with a 10-pL cartridge (Fujifilm Dimatix, DMC-11610) having a nozzle diameter of 21 µm was used for the inkjet printing. A slightly modified preprogrammed inverted trapezoid waveform with a jetting voltage of 16–18 V and a maximum jetting frequency of 5 kHz was utilized for the ink deposition. A typical working distance between the nozzle and the substrate is 1 mm. Drop spacing was optimized to be 40 µm for MoS_2 flake deposition and 30 µm for graphene flake deposition onto the substrates that were heated to 50 °C. To fabricate an FET water sensor, the MoS_2 channel was first printed followed by four layers of graphene electrode deposition. The MoS_2 channel length was 400 µm between the source and drain electrodes. The resulting devices were annealed at 350 °C for 1 h in Ar gas to remove residual additives in the inks and improve the junction contacts of the entire devices. The graphene sensing area was then functionalized with 1-pyrenebutyric acid through N,N-Dimethylmethanamidesolution (DMF) solution (100 mM) incubation at room temperature for 1 h to obtain the fully functioning inkjet-printed water sensor, which can be used for lead ion detection. The electrical properties and sensing performance of the resulting water sensors were characterized by a Keithley 4200A-SCS semiconductor characterization system under ambient conditions. A narrow top V_g window within ± 0.5 V was applied to avoid electrolysis during the sensing test.

Characterization: Scanning electron microscopy (SEM) and optical microscopy were performed using a JEOL JSM-7500 (FE) SEM and OMAX Infinity Trinocular Metallurgical Microscope, respectively. Raman spectroscopy was measured using an inVia InSpect confocal Raman microscope with a 532-nm laser source. Thermogravimetric analysis (TGA) was conducted with a Mettler Toledo TGA/DSC 3+ under an argon flow (50 mL min^{-1}) at a heating rate of 7.5 °C min^{-1} from room temperature to 800 °C. Atomic force microscopy (AFM) was measured with a Bruker ICON System.

Supporting Information

Supporting Information is available from the Wiley Online Library or from the author.

Acknowledgements

This work was primarily supported by the National Science Foundation Scalable Nanomanufacturing Program (NSF CMMI-1727846 and NSF CMMI-2039268) and the Future Manufacturing Research Grant Program (NSF CMMI-2037026). This work was also supported by the Laboratory Directed Research and Development (LDRD) program from Argonne National Laboratory, provided by the Director, Office of Science, of the U.S. Department of Energy under Contract No. DE-AC02-06CH11357. Use of the Center for Nanoscale Materials, an Office of Science user facility, was supported by the U.S. Department of Energy, Office of Science, Office of Basic Energy Sciences, under Contract No. DE-AC02-06CH11357. This study also utilized instrumentation within the Northwestern University NUANCE Center, which is supported by the Soft and Hybrid Nanotechnology Experimental (ShyNE) Resource (NSF ECCS-2025633), the International Institute for Nanotechnology (IIN), and the Northwestern University Materials Research Science and Engineering Center (MRSEC) program (NSF DMR-1720139).

Conflict of Interest

J.H.C. has financial interests in NanoAffix Science LLC. The company did not fund this work. All other authors declare no competing interests.

Data Availability Statement

The data that support the findings of this study are available from the corresponding author upon reasonable request.

Keywords

additive manufacturing, coffee-ring effects, graphene, MoS_2, thin-film transistors

Received: August 3, 2023
Published online:

[1] X. Y. Sui, J. R. Downing, M. C. Hersam, J. H. Chen, *Mater. Today* **2021**, *48*, 135.
[2] J. Chen, H. Pu, M. C. Hersam, P. Westerhoff, *Adv. Mater.* **2022**, *34*, 2106975.
[3] Q. Qiu, Z. Huang, *Adv. Mater.* **2021**, *33*, 2008126.
[4] P. Fathi-Hafshejani, N. Azam, L. Wang, M. A. Kuroda, M. C. Hamilton, S. Hasim, M. Mahjouri-Samani, *ACS Nano* **2021**, *15*, 11461.
[5] A. Maity, X. Sui, H. Pu, K. J. Bottum, B. Jin, J. Chang, G. Zhou, G. Lu, J. Chen, *Nanoscale* **2020**, *12*, 1500.
[6] D. Xiang, T. Liu, J. Xu, J. Y. Tan, Z. Hu, B. Lei, Y. Zheng, J. Wu, A. H. C. Neto, L. Liu, W. Chen, *Nat. Commun.* **2018**, *9*, 2966.
[7] T. De Silva, M. Fawzy, A. Hasani, H. Ghanbari, A. Abnavi, A. Askar, Y. Ling, M. R. Mohammadzadeh, F. Kabir, R. Ahmadi, M. Rosin, K. L. Kavanagh, M. M. Adachi, *Nat. Commun.* **2022**, *13*, 7593.
[8] M. M. Luo, T. J. Fan, Y. Zhou, H. Zhang, L. Mei, *Adv. Funct. Mater.* **2019**, *29*, 1808306.
[9] M. T. Hwang, M. Heiranian, Y. Kim, S. You, J. Leem, A. Taqieddin, V. Faramarzi, Y. Jing, I. Park, A. M. van der Zande, S. Nam, N. R. Aluru, R. Bashir, *Nat. Commun.* **2020**, *11*, 1543.
[10] A. Dodda, D. Jayachandran, A. Pannone, N. Trainor, S. P. Stepanoff, M. A. Steves, S. S. Radhakrishnan, S. Bachu, C. W. Ordonez, J. R. Shallenberger, J. M. Redwing, K. L. Knappenberger, D. E. Wolfe, S. Das, *Nat. Mater.* **2022**, *21*, 1379.
[11] T. Y. Kim, J. Ha, K. Cho, J. Pak, J. Seo, J. Park, J. K. Kim, S. Chung, Y. Hong, T. Lee, *ACS Nano* **2017**, *11*, 10273.
[12] Z. Wang, K. Yi, Q. Lin, L. Yang, X. Chen, H. Chen, Y. Liu, D. Wei, *Nat. Commun.* **2019**, *10*, 1544.
[13] O. A. Moses, L. B. Gao, H. T. Zhao, Z. Wang, M. L. Adam, Z. H. Sun, K. L. Liu, J. H. Wang, Y. Lu, Z. Y. Yin, X. F. Yu, *Mater. Today* **2021**, *50*, 116.
[14] D. McManus, S. Vranic, F. Withers, V. Sanchez-Romaguera, M. Macucci, H. Yang, R. Sorrentino, K. Parvez, S. K. Son, G. Iannaccone, K. Kostarelos, G. Fiori, C. Casiraghi, *Nat. Nanotechnol.* **2017**, *12*, 343.
[15] L. Kuo, V. K. Sangwan, S. V. Rangnekar, T. C. Chu, D. Lam, Z. Zhu, L. J. Richter, R. Li, B. M. Szydlowska, J. R. Downing, B. J. Luijten, L. J. Lauhon, M. C. Hersam, *Adv. Mater.* **2022**, *34*, 2203772.
[16] D. C. Moore, A. Jawaid, R. Busch, M. Brothers, P. Miesle, A. Miesle, R. Rao, J. Lee, L. K. Beagle, M. Motala, S. G. Wallace, J. R. Downing, A. Roy, C. Muratore, M. C. Hersam, R. Vaia, S. Kim, N. R. Glavin, *Adv. Funct. Mater.* **2021**, *32*, 2106830.

[17] C. C. Pola, S. V. Rangnekar, R. Sheets, B. M. Szydlowska, J. R. Downing, K. W. Parate, S. G. Wallace, D. Tsai, M. C. Hersam, C. L. Gomes, J. C. Claussen, *2D Mater.* **2022**, *9*, 035016.
[18] J. T. Seo, J. Zhu, V. K. Sangwan, E. B. Secor, S. G. Wallace, M. C. Hersam, *ACS Appl. Mater. Interfaces* **2019**, *11*, 5675.
[19] Z. Lin, Y. Liu, U. Halim, M. Ding, Y. Liu, Y. Wang, C. Jia, P. Chen, X. Duan, C. Wang, F. Song, M. Li, C. Wan, Y. Huang, X. Duan, *Nature* **2018**, *562*, 254.
[20] J. Kim, D. Rhee, O. Song, M. Kim, Y. H. Kwon, D. U. Lim, I. S. Kim, V. Mazanek, L. Valdman, Z. Sofer, J. H. Cho, J. Kang, *Adv. Mater.* **2022**, *34*, 2106110.
[21] T. Carey, A. Arbab, L. Anzi, H. Bristow, F. Hui, S. Bohm, G. Wyatt-Moon, A. Flewitt, A. Wadsworth, N. Gasparini, J. M. Kim, M. R. Lanza, I. McCulloch, R. Sordan, F. Torrisi, *Adv. Electron. Mater.* **2021**, *7*, 2100112.
[22] A. G. Kelly, T. Hallam, C. Backes, A. Harvey, A. S. Esmaeily, I. Godwin, J. Coelho, V. Nicolosi, J. Lauth, A. Kulkarni, S. Kinge, L. D. Siebbeles, G. S. Duesberg, J. N. Coleman, *Science* **2017**, *356*, 69.
[23] M. J. Zhang, Y. Li, X. D. Li, N. Y. Wang, C. S. Huang, *Adv. Electron. Mater.* **2020**,*6*, 2000157.
[24] S. Chung, K. Cho, T. Lee, *Adv. Sci.* **2019**, *6*, 1801445.
[25] D. Mampallil, H. B. Eral, *Adv. Colloid Interface Sci.* **2018**, *252*, 38.
[26] S. K. Mondal, A. Biswas, J. R. Pradhan, S. Dasgupta, *Small Methods* **2021**, *5*, 2100634.
[27] O. Song, D. Rhee, J. Kim, Y. Jeon, V. Mazanek, A. Soll, Y. A. Kwon, J. H. Cho, Y. H. Kim, J. Kang, Z. Sofer, *npj 2D Mater. Appl.* **2022**, *6*, 64.
[28] F. Torrisi, T. Hasan, W. Wu, Z. Sun, A. Lombardo, T. S. Kulmala, G. W. Hsieh, S. Jung, F. Bonaccorso, P. J. Paul, D. Chu, A. C. Ferrari, *ACS Nano* **2012**, *6*, 2992.
[29] G. Hu, L. Yang, Z. Yang, Y. Wang, X. Jin, J. Dai, Q. Wu, S. Liu, X. Zhu, X. Wang, T. C. Wu, R. C. T. Howe, T. Albrow-Owen, L. W. T. Ng, Q. Yang, L. G. Occhipinti, R. I. Woodward, E. J. R. Kelleher, Z. Sun, X. Huang, M. Zhang, C. D. Bain, T. Hasan, *Sci. Adv.* **2020**, *6*, eaba5029.
[30] A. A. Pahlavan, L. Yang, C. D. Bain, H. A. Stone, *Phys. Rev. Lett.* **2021**, *127*, 024501.
[31] Y. Shao, J. H. Fu, Z. Cao, K. Song, R. Sun, Y. Wan, A. Shamim, L. Cavallo, Y. Han, R. B. Kaner, V. C. Tung, *ACS Nano* **2020**, *14*, 7308.
[32] G. Hu, T. Albrow-Owen, X. Jin, A. Ali, Y. Hu, R. C. T. Howe, K. Shehzad, Z. Yang, X. Zhu, R. I. Woodward, T. C. Wu, H. Jussila, J. B. Wu, P. Peng, P. H. Tan, Z. Sun, E. J. R. Kelleher, M. Zhang, Y. Xu, T. Hasan, *Nat. Commun.* **2017**, *8*, 278.
[33] O. Ogbeide, G. Bae, W. B. Yu, E. Morrin, Y. Y. Song, W. Song, Y. Li, B. L. Su, K. S. An, T. Hasan, *Adv. Funct. Mater.* **2022**, *32*, 2113348.
[34] K. F. Mak, C. Lee, J. Hone, J. Shan, T. F. Heinz, *Phys. Rev. Lett.* **2010**, *105*, 136805.
[35] K. K. Liu, W. Zhang, Y. H. Lee, Y. C. Lin, M. T. Chang, C. Y. Su, C. S. Chang, H. Li, Y. Shi, H. Zhang, C. S. Lai, L. J. Li, *Nano Lett.* **2012**, *12*, 1538.
[36] S. Ippolito, A. G. Kelly, R. Furlan de Oliveira, M. A. Stoeckel, D. Iglesias, A. Roy, C. Downing, Z. Bian, L. Lombardi, Y. A. Samad, V. Nicolosi, A. C. Ferrari, J. N. Coleman, P. Samori, *Nat. Nanotechnol.* **2021**, *16*, 592.
[37] J. Acharya, J. Wilt, B. Liu, J. Wu, *ACS Appl. Mater. Interfaces* **2018**, *10*, 3112.
[38] L. Kong, G. Li, Q. Su, X. Zhang, Z. Liu, G. Liao, B. Sun, T. Shi, *Adv. Eng. Mater.* **2023**, *25*, 2200946.
[39] X. Y. Sui, H. H. Pu, A. Maity, J. B. Chang, B. Jin, G. H. Lu, Y. L. Wang, R. Ren, S. Mao, J. H. Chen, *ECS J. Solid State Sci. Technol.* **2020**, *9*, 115012.
[40] E. B. Secor, P. L. Prabhumirashi, K. Puntambekar, M. L. Geier, M. C. Hersam, *J. Phys. Chem. Lett.* **2013**, *4*, 1347.
[41] E. B. Secor, J. Smith, T. J. Marks, M. C. Hersam, *ACS Appl. Mater. Interfaces* **2016**, *8*, 17428.
[42] E. B. Secor, B. Y. Ahn, T. Z. Gao, J. A. Lewis, M. C. Hersam, *Adv. Mater.* **2015**, *27*, 6683.
[43] D. Song, A. Mahajan, E. B. Secor, M. C. Hersam, L. F. Francis, C. D. Frisbie, *ACS Nano* **2017**, *11*, 7431.
[44] W. J. Hyun, E. B. Secor, C. H. Kim, M. C. Hersam, L. F. Francis, C. D. Frisbie, *Adv. Energy Mater.* **2017**, *7*, 1700285.
[45] K. Schauble, D. Zakhidov, E. Yalon, S. Deshmukh, R. W. Grady, K. A. Cooley, C. J. McClellan, S. Vaziri, D. Passarello, S. E. Mohney, M. F. Toney, A. K. Sood, A. Salleo, E. Pop, *ACS Nano* **2020**, *14*, 14798.
[46] Y. Hao, Y. Wang, L. Wang, Z. Ni, Z. Wang, R. Wang, C. K. Koo, Z. Shen, J. T. Thong, *Small* **2010**, *6*, 195.
[47] S. H. Kim, K. Hong, W. Xie, K. H. Lee, S. Zhang, T. P. Lodge, C. D. Frisbie, *Adv. Mater.* **2013**, *25*, 1822.
[48] S. Rathi, I. Lee, D. Lim, J. Wang, Y. Ochiai, N. Aoki, K. Watanabe, T. Taniguchi, G. H. Lee, Y. J. Yu, P. Kim, G. H. Kim, *Nano Lett.* **2015**, *15*, 5017.
[49] S. S. Chee, D. Seo, H. Kim, H. Jang, S. Lee, S. P. Moon, K. H. Lee, S. W. Kim, H. Choi, M. H. Ham, *Adv. Mater.* **2019**, *31*, 1804422.
[50] C. J. Shih, Q. H. Wang, Y. Son, Z. Jin, D. Blankschtein, M. S. Strano, *ACS Nano* **2014**, *8*, 5790.
[51] F. Chai, C. Wang, T. Wang, L. Li, Z. Su, *ACS Appl. Mater. Interfaces* **2010**, *2*, 1466.